Article Type: Research Article

Dose volume histogram-based optimization of image reconstruction parameters for quantitative ^{90}Y-PET imaging

Wendy Siman[1,2], Justin K. Mikell[3], Osama R. Mawlawi[4,5], Firas Mourtada[6], S. Cheenu Kappadath[4,5]

[1]*Department of Radiology, The University of Tennessee Medical Center, Knoxville, TN, USA*

[2]*The University of Tennessee Graduate School of Medicine, Knoxville, TN, USA*

[3]*Department of Radiation Oncology, University of Michigan Hospital and Health Systems, Ann Arbor, MI, USA*

[4]*Department of Imaging Physics, The University of Texas MD Anderson Cancer Center, Houston, TX, USA*

[5]*The University of Texas Graduate School of Biomedical Sciences at Houston, Houston, TX, USA*

[6]*Christiana Care Hospital, Newark, DE, USA*

Running Title: DVH optimization of quantitative ^{90}Y-PET

Corresponding Author: S. Cheenu Kappadath, Ph.D.
Department of Imaging Physics
The University of Texas MD Anderson Cancer Center
1155 Pressler St., Unit 1352
Houston, TX 77030, USA
Phone: 713-745-2835
Fax: 713-563-8842
Email: skappadath@mdanderson.org

This is the author manuscript accepted for publication and has undergone full peer review but has not been through the copyediting, typesetting, pagination and proofreading process, which may lead to differences between this version and the Version of Record. Please cite this article as doi: 10.1002/mp.13269

Abstract

Purpose: ^{90}Y-microsphere radioembolization or selective internal radiation therapy is increasingly being used as a treatment option for tumors that are not candidates for surgery and external beam radiation therapy. Recently, volumetric ^{90}Y dosimetry techniques have been implemented to explore tumor dose response on the basis of 3D ^{90}Y-activity distribution from PET imaging. Despite being a theranostic study, the optimization of quantitative ^{90}Y-PET image reconstruction still uses the mean activity concentration recovery coefficient as the objective function, which is more relevant to diagnostic and detection tasks than is dosimetry. The aim of this study was to optimize ^{90}Y-PET image reconstruction by minimizing errors in volumetric dosimetry via the dose volume histogram (DVH). We propose a joint optimization of the number of equivalent iterations (the product of the iteration and subsets) and the post-reconstruction filtration (FWHM) to improve the accuracy of voxel-level ^{90}Y dosimetry.

Methods: A modified NEMA IEC phantom was used to emulate clinically relevant ^{90}Y-PET imaging conditions through various combinations of acquisition durations, activity concentrations, sphere-to-background ratios, and sphere diameters. PET data were acquired in list mode for 300 min in a single-bed position; we then rebinned the list mode PET data to 60, 45, 30, 15, and 5 min per bed, with 10 different realizations. Errors in the DVH were calculated as root mean square errors (RMSEs) of the differences in the image-based sphere DVH and the expected DVH. The new optimization approach was tested in a phantom study, and the results were compared with the more commonly used objective function of the mean-activity-concentration recovery coefficient.

Results: In a wide range of clinically relevant imaging conditions, using 36 equivalent iterations with 5.2-mm filtration resulted in a decreased number of systematic errors in volumetric ^{90}Y dosimetry, quantified as image-based DVH, in ^{90}Y-PET images reconstructed using the OSEM iterative reconstruction with TOF and PSF modeling. Our proposed objective function of minimizing errors in DVH, which allows for joint optimization of ^{90}Y-PET iterations and filtration for volumetric quantification of the ^{90}Y dose, may be superior to conventional recovery coefficient-based approaches.

Conclusion: Our proposed objective function of minimizing errors in DVH, which allows for joint optimization of iterations and filtration to reduce errors in the PET-based volumetric quantification ^{90}Y dose, is relevant to dosimetry in therapy procedures. The proposed optimization method using DVH as the objective function could be applied to any imaging modality used to assess voxel-level quantitative information.

Key words: ^{90}Y, PET, dosimetry, optimization, dose volume histogram, quantitative

1. INTRODUCTION

Selective internal radiation therapy (SIRT) using ^{90}Y-microspheres, also referred to as ^{90}Y-radioembolization, is a loco-regional liver-directed therapy for non-resectable liver cancer.[1–5] During ^{90}Y-radioembolization, radioactive ^{90}Y-microspheres (~30 μm in size) are delivered intra-arterially to liver tumors for permanent implantation. Because of their embolic size, the microspheres become trapped in the microvasculature of tumor capillary vessels. The radioactive beta particle emissions from trapped ^{90}Y-microspheres deliver high radiation doses to proximal tissue (tumors) while sparing distal tissue (normal liver).

Initially, ^{90}Y-microsphere therapy was used primarily for palliative care; therefore, ^{90}Y-SIRT treatment planning focused only on minimizing normal liver toxicity. To date, the package insert dosimetry model for treatment planning with commercially available ^{90}Y-microsphere devices assumes a uniform distribution of microspheres in the treatment volume (that includes tumors and normal liver tissue).[6–8] This simplistic model typically underestimates the radiation dose to the tumor and overestimates the dose to the normal liver.[9] Partition model dosimetry was proposed as an alternative to overcome the limitation of uniform activity distribution within the liver by accounting for the preferential (higher) uptake in tumors but still assuming uniform uptake within the tumor and normal liver compartments.[10] The ideal scenario for partition model dosimetry is a single tumor and uniform uptake in both tumor and normal liver regions. However, the accuracy and validity of partition model dosimetry is tenuous in the presence of multiple lesions with varied uptake or non-uniform uptake in the normal liver compartment (as is the typical clinical scenario).[9,11] Nonetheless, partition model dosimetry has been used by a number of investigators to better separate radiation-absorbed dose estimates between the tumor and normal liver compartments.[12–14] It has been reported in numerous clinical practices that patients who received ^{90}Y-SIRT had better clinical outcomes, including better local control and overall survival, than did those who received supportive palliative care.[15–17] Furthermore, a correlation between tumor dose and tumor response has been reported.[12,14,15,18] The observed improvement in survival (albeit in retrospective studies in most cases) and evolving knowledge on the tumor-dose response have shifted the treatment planning paradigm from safety to a front-line therapy aimed at elucidating a tumor response.

While estimation of the mean organ absorbed doses is sufficient for palliative treatment planning, the dosimetry task for delivering ^{90}Y-SIRT with a therapeutic intent should aim to calculate the normal tissue complication probability and tumor control probability for the individual therapy plan (as is done routinely in radiation oncology treatment planning). Accurate determination of these 2 end points requires volumetric information on the absorbed dose distribution for the tumor and normal liver tissue;[19–21] therefore, there is an acute need for accurate quantitative 3D dosimetry of ^{90}Y-SIRT and the establishment of absorbed dose response characteristics for both tumors and organs at risk, such as the liver and lungs.

Volumetric ^{90}Y dosimetry techniques have been implemented on the basis of 3D ^{90}Y activity distribution from both ^{90}Y-bremsstrahlung SPECT/CT[11,22,23] and ^{90}Y-PET/CT[24–27] imaging. It has also been shown that the local deposition method can be used to generate a ^{90}Y absorbed dose map (Gy) by

scaling the quantitative SPECT or PET images (Bq/mL) using a single conversion factor (Gy.mL/Bq).[11,26,28,29] The 3D dose distribution on the SPECT- or PET-based ^{90}Y dose map can be quantified using the dose volume histogram (DVH).[27,28,30,31] The DVH is a plot of the threshold dose in the abscissa against the fraction of the volume of interest (VOI), with the dose greater than or equal to the threshold dose in the ordinate. The conventional summary metrics, such as the minimum, maximum, and median doses, can also be retrieved from the DVH. The ordinate of the DVH ranges from 0% to 100%, and the slope of the DVH curve around the median is indicative of the degree of uniformity of the 3D dose distribution in the VOI.

^{90}Y-PET imaging poses unique challenges, primarily due to the extremely low positron yield of 32 x 10^{-6} in the ^{90}Y decay process.[32] As a comparison, the positron yield in the ^{18}F decay process is 97 x 10^{-2}. To compensate for the low signal, ^{90}Y-PET images are typically acquired for 20–30 min/bed instead of the usual 2-3 min/bed in the ^{18}FDG-PET study. During ^{90}Y-radioembolization, about 3 GBq (80 mCi) of ^{90}Y microspheres are deposited in the liver. In contrast, for the ^{18}FDG-PET study, about 370 MBq (10 mCi) of ^{18}FDG is distributed in the whole body. The true coincidence counts acquired per bed position in ^{90}Y-microsphere PET imaging are therefore up to 100 times lower than the true coincidence counts acquired by ^{18}FDG-PET imaging. Therefore, the performance characteristics of reconstructed ^{90}Y-PET images at such low signal levels, in terms of the image quality (noise and artifacts) and quantitation (accuracy and precision), are not well understood, unlike those for ^{18}FDG-PET images.

Image noise and partial volume effect are major degrading factors that limit the accuracy of voxel-based dosimetry.[19] Furthermore, there has been no standardization of the data acquisition and image reconstruction schemas for ^{90}Y-PET imaging.[33] In routine clinical implementation, the iterative reconstruction parameters are chosen by balancing quantitative accuracy with image noise and reconstruction time. The typical approach in iterative reconstruction is to iterate so as to clearly visualize large tumors and then apply filtration to smooth the final image. Recent studies of OSEM reconstruction parameter optimization for quantitative ^{90}Y-PET imaging used the mean activity concentration recovery coefficient (RC) as the objective function.[34–38] While an increase in the number of equivalent iterations (defined as the product of iterations and subsets) improves the image resolution and accuracy of the mean activity concentration, it also increases the image noise.[39] As a further complication, the degree of convergence with iterative reconstruction approaches depends on a large number of parameters, including the sphere size and the sphere-to-background ratio (SBR). After convergence is achieved, an increase in the number of equivalent iterations only results in higher image noise. The usual practice of using post-reconstruction filtration (e.g., Gaussian) to reduce image noise leads to an underestimation of the mean activity concentration to a severe degree, depending on the magnitude of the filter (i.e., the full-width at half-maximum [FWHM]). Therefore, we posit that the RC is not well suited as the objective function for the optimization of reconstruction related to dosimetry and DVH quantitation.

Our long-term goal is to perform a systematic investigation of the bias and variability in ^{90}Y-PET-based absorbed dose quantification; this effort has been separated into 2 parts. In this study, the scope of

our work was to develop an appropriate metric for assessing the performance of ^{90}Y-PET for absorbed dose quantification. Specifically, the objective was not to evaluate the performance of ^{90}Y-PET dose quantification but to introduce an appropriate metric to assess its performance. We propose a joint optimization of the ^{90}Y-PET image reconstruction protocol (i.e., the number of equivalent iterations and the post-reconstruction filtration FWHM) to improve the accuracy of voxel-level 3D volumetric ^{90}Y dosimetry from count-starved ^{90}Y-PET images by directly interrogating the errors in the resultant DVH. The performance of ^{90}Y-PET image reconstruction was also evaluated using the traditional RC of the mean sphere dose. We report on the optimization of the ^{90}Y-PET image reconstruction protocol in a phantom using a modified NEMA IEC phantom study under a wide range of clinically relevant imaging conditions: sphere sizes, activity concentrations, SBRs, and acquisition durations.

In a subsequent study, we will use the metric proposed here to investigate the numerous variables related to introducing errors in the performance of ^{90}Y-PET-based dose quantification (for example, image counts, image count rate, sphere size, sphere dose, SBR, and background signal).

2. METHODS

2.A. Data acquisition and phantom description

A modified NEMA IEC phantom (Biodex, Shirley, NY) was used to emulate clinically relevant ^{90}Y PET imaging conditions through various combinations of acquisition durations, activity concentrations, sphere-to-background ratios (SBRs), and sphere diameters. The modified IEC phantom contained 2 sphere sets of 37, 17, and 13 mm diameters each. These spheres were filled with ^{90}Y AC of 4.8 MBq/mL (130 uCi/mL) and 1.6 MBq/mL (43 uCi/mL); the background chamber was filled with 0.4 MBq/mL (10 uCi/mL) to give SBRs of 13 and 4 for the 2 sphere sets.

PET data for the IEC phantom were acquired in list mode using a GE D690 PET/CT scanner (General Electric, Milwaukee, WI) for 300 min in a single-bed position. The ^{90}Y radionuclide was programmed into the scanner with a half-life of 64.1 h and a branching ratio of $32x10^{-6}$. The spheres were positioned at the center of the PET axial field of view (FOV). We replayed the list mode PET data to 60, 45, 30, 15, and 5 min per bed to evaluate the potential variation of optimum reconstruction parameters under a range of signal conditions. Furthermore, by taking advantage of the list mode acquisition, each reconstruction was performed using 10 different realizations. The DVH and RC values reported were based on the average of the 10 different realizations to diminish the impact of the statistical (random) noise. The reported behavior would then mainly be affected by uncertainties stemming from the reconstruction algorithm and the system spatial resolution. In addition to the initial day 0 acquisition described, we reacquired the PET data in list mode on day 3 when the sphere ACs had decayed to 2.3 and 0.8 MBq/mL to assess the potential variation in optimal reconstruction parameters due to the count rate during acquisition.

PET/CT images were reconstructed using the 3D Ordered Subset Expectation Maximization (3D OSEM) algorithm with point spread function (PSF) and time of flight (TOF) modeling (GE VPFXS). The

number of iterations varied from 1–12, while the number of subsets was fixed at 12; this resulted in equivalent iterations that ranged from 12 to 144. Post-reconstruction Gaussian filters were applied in the transaxial plane; the FWHM of the filters was 0, 2.6, 5.2, 7.8, or 10.4 mm. The voxel size was 2.6 × 2.6 × 3.3 mm^3. All reconstructed ^{90}Y PET images (the activity concentration map in Bq/mL) were multiplied by a scaling factor of 4.78×10^{-5} Gy.mL/Bq to convert them to a ^{90}Y dose map (Gy) via the local deposition method (LDM).[26] The corresponding absorbed doses of the sphere sets were 230 and 77 Gy on days 0 and 110, respectively, and 37 Gy on day 3.

2.B. DVH optimization

The 3D ^{90}Y dose distribution in the hot spheres was investigated using DVH.[27] The sphere DVHs were calculated from the sphere VOIs in the PET images. These sphere VOIs were defined on the basis of the segmentation of their corresponding CT images, as demonstrated in Fig 1 for 37- and 17-mm spheres with SBRs of 13.

Two objective metrics were used to evaluate the quantitative ^{90}Y PET image reconstruction: 1) minimization of the errors in the sphere DVH and 2) maximization of the RC for the mean sphere dose. Errors in the DVH were calculated as root mean square errors (RMSEs) of the differences in the image-based sphere DVH and the reference DVH, i.e., $RMSE = \sqrt{\frac{\sum_{20}^{80}(D_x - D_{x,ref})^2}{60}}$. Here, D_x is the PET image-based DVH at x% volume coverage, whereas $D_{x,ref}$ is the expected DVH at x% volume coverage on the basis of the phantom setup. The PET-based DVHs in this study were based on 3D ^{90}Y dose distributions that had been determined using the LDM on PET images that converted 3D AC distributions into 3D absorbed dose distributions. The corresponding reference 3D absorbed dose and DVH distributions were calculated using the dose point kernel (DPK) convolution method.[26,40,41] Using isotropic 2.21-mm voxels and the corresponding voxel S-values from Lanconelli *et al*,[41] we applied DPK convolution to the known ^{90}Y activity concentration in the spheres and background to obtain the reference 3D absorbed dose. The dose kernels we used from Lanconelli *et al* account for the beta spectra–they simulate several monoenergetic betas and then weight the spectra accordingly. The reference DVHs were not calculated from PET images; thus, they were degraded by neither PET image noise nor resolution. The limiting resolution in our reference DVH was the voxel size, which was set to an isotropic 2.21 mm.

DPK is a voxel dosimetry technique that uses voxel S-values[41,42] for ^{90}Y and can account for the exchange of energy deposition at the sphere boundary due to electron transport. The β^- particles emitted during ^{90}Y decay have a maximum energy of 2.28 MeV, a mean tissue penetration of 2.5 mm, and a maximum range of 1.1 cm. Therefore, some of the β^- particles from ^{90}Y disintegrations near the sphere boundary may exit the sphere and deposit energy in the background medium, leading to a lower absorbed dose at the peripheral voxels of the spheres. Consequently, the reference DVHs are not straight vertical lines. We compared the reference DVH against the DVH realized by ^{90}Y PET images to

assess scanner performance. Therefore, no additional modeling of the PET system resolution or other degradation factors was applied to the reference DVHs.

RMSEs were calculated from D_{80} to D_{20} to avoid high errors near the maximum (D_0) and minimum (D_{100}) doses due to high image noise in the count-starved ^{90}Y PET study.[27] The RMSE for each sphere DVH was calculated as an average of 10 different image noise realizations; the standard errors were reported. RMSEs were calculated for all image-reconstruction-parameter combinations (the number of equivalent iterations and the filtration FWHM).

To determine the sensitivity of RMSEs to the selection of dose threshold ranges, we also investigated RMSE trends as a function of dose threshold ranges: D_0–D_{100}, D_{10}–D_{90}, D_{20}–D_{80}, D_{30}–D_{70}, D_{50}–D_{80}, and D_{60}–D_{90}.

2.C. RC convergence method

As a comparison, the reconstruction parameters were also optimized using the conventional objective function of the sphere RC, calculated as $RC = D_{mean}/D_{true}$, where, D_{mean} is the mean dose in the sphere calculated from CT-contoured VOI, and D_{true} is the known absorbed dose in the sphere calculated using the LDM with the known ^{90}Y activity concentration. Here again, the sphere RC were calculated as an average of 10 different image noise realizations. The convergence properties of the sphere RC were evaluated under the various aforementioned imaging conditions. For optimization using RC convergence, no post-reconstruction filtration was applied to PET images because the application of any smoothing filter will increase the partial volume effect and decrease the RC;[33,43,44] hence, in this study, RC convergence was only determined by calculating the sphere RC as a function of the number of equivalent iterations.

3. RESULTS

3.A. DVH optimization

Images of the modified IEC phantom (day 0, 15-min acquisition), reconstructed for different numbers of equivalent iterations (12–48) but with a fixed filtration of 5.2-mm FWHM, are shown in Fig 2A; note the increase in image noise with the higher number of equivalent iterations. The same data (day 0, 15-min acquisition) reconstructed for a fixed number of 36 equivalent iterations but different filtrations (2.6–10.4-mm FWHM) are shown in Fig 2B; note the decrease in image noise with the higher amount of filtration. The corresponding DVHs of the 17-mm sphere (day 0, 15-min acquisition, SBR of 13, dose of 230 Gy) are shown in Fig 2C and Fig 2D as a function of the number of equivalent iterations and filtration FWHM, respectively. The increase in image noise with higher equivalent iterations and lower filtrations widens the distribution in the DVH profile, especially at the higher voxel doses (i.e., bottom right region).

The solid black curves in Fig 2C and Fig 2D indicate the reference DVH, calculated using the DPK convolution method. Although the activity concentrations in the spheres are uniform, some of the β-particles from ^{90}Y disintegrations near the sphere boundary exit the sphere and deposit energy in the

background medium, leading to a lower absorbed dose at the peripheral voxels of the spheres; hence, the reference DVHs are not straight vertical lines.

The RMSEs of the image-based DVH for the 17-mm sphere (day 0, 15 min acquisition, 13 SBR, 230 Gy dose), as a function of equivalent iterations (corresponding to Fig 2C) and filtration FWHM (corresponding to Fig 2D), are shown in Fig 3. The standard errors of selected DVH RMSEs are also shown as the error bars. The small error bars indicate that the RMSE curves in Fig 3 are minimally influenced by stochastic noise. The RMSEs of DVH were among the lowest around 36 equivalent iterations; a further increase in the number of equivalent iterations resulted in higher noise, as evidenced by the increased spread of DVH (Fig 2C) and increased RMSEs (Fig 2), which was more apparent in images with less filtration. Similarly, the RMSE of the DVH was the lowest at a filtration of 5.2 mm FWHM; heavier filtration shifted the DVH toward lower doses and resulted in a higher underestimation of DVH (Fig 2D).

Similar RMSE behavior was observed at different dose levels for the 17-mm sphere at a dose of 37 Gy (Fig 3B) and for different sphere sizes and doses (Fig 2C and Fig 2D). The DVH RMSE in a larger sphere image (37 mm in diameter) was the lowest at an equivalent iteration of 24, while the RMSE in a smaller sphere image (13 mm in diameter) was the lowest at 48 equivalent iterations. However, image reconstruction of all spheres (diameter of 37–13 mm) using 36 equivalent iterations resulted in a change of absolute errors in the DVH of < 1% at all volume coverages.

As the sphere image noise (or dose non-uniformity) increased due to lower dose or shorter duration, 7.8-mm filtration resulted in lower RMSEs of DVH than did 5.2-mm filtration. Changes in the mean dose (nominal 77 Gy) for the 17-mm sphere DVH, calculated from sphere images (day 0, 15 min acquisition) with 5.2 and 7.8-mm filtration, were < 3% at volume coverage of 20%–80%, on average.

While the use of image filtration suppresses image noise and hence reduces noise-dependent errors in DVH, it also increases the errors in DVH due to increased partial volume effect. Heavier filtration with FWHM of 7.8 and 10.4 mm could be used on a larger sphere (37-mm sphere), where partial volume effect is less severe, to further reduce the RMSE of DVH estimate; however, filtration beyond 7.8 mm FWHM did not significantly improve the DVH (< 2% absolute change at all volume coverage). In contrast, the use of filtration with FHWM wider than 5.2 mm increased the RMSE of DVH in smaller spheres, e.g., the in 17-mm sphere (Fig 2D and Fig 3). We found that images reconstructed using equivalent iterations of 24–48 and filtrations of 5.2–7.8 mm FWHM yielded RMSEs of sphere DVH that were consistently among the lowest in various tested imaging conditions.

The RMSEs calculated using the entire dose threshold range, from D_0-D_{100}, increased monotonically with a higher number of equivalent iterations (Fig 4). This increase in noise may be related to the fact that 1) image noise increases with a higher number of equivalent iterations and 2) high noise levels were observed at both the low and high DVH coverages (see Fig 2). Consequently, when the extrema of DVH were excluded in the calculation of the RMSE, such as D_{20}-D_{80} and D_{30}-D_{70}, we observed an initial decrease in the RSME before the monotonic increase with equivalent iterations, as

shown in Fig 4. RMSE trends, when the very low and the very high dose coverages were excluded, were similar, as a function of equivalent iterations—i.e., RMSEs were the lowest at 36 equivalent iterations with 5.2-mm filtration (Fig 4). We chose a dose threshold range of D_{20}-D_{80} as a conservative approach to avoid noise-related errors near the extremes, which cause high errors (Fig 2).

3.B. RC convergence method

The converged RC value was seen to depend on the scan duration, with lower RC observed for shorter durations (Fig 5A). The spread in converged RC values, as a function of the scan duration, increased with the decrease in sphere sizes; RC values of 70%-75% (spread of 5%) were observed for the 37-mm sphere with a 15-60 min/bed that increased to 35%-50% (spread of 15%) for the 13-mm sphere (Fig 5A). The converged value of RC decreased with smaller sphere sizes, ranging from 75% for 34 mm spheres to 55% for 13-mm spheres (Fig 5B). The converged value, however, was largely insensitive to the SBR and sphere dose (Fig 5B).

The convergence rates were found to be higher at the higher dose level. Fig 5C shows faster RC convergence for both the 34- and 17-mm spheres at 230 Gy compared to the rates observed when the activity in the spheres had decreased to 64 Gy. The rate of convergence for RC was largely insensitive to sphere sizes, SBRs, and acquisition duration, as shown in Fig 5A and Fig 5B. Overall, spheres with various imaging conditions achieved RC convergence after 36 equivalent iterations.

4. DISCUSSION

The goal of ^{90}Y PET is not tumor detection but rather estimation of the radiation dose delivered to the tumor (at the voxel level). Therefore, the accuracy of the PET image in terms of the quantitative pixel value in Bq/mL is of the highest relevance. As the number of equivalent iterations increases, the sphere activity concentration (or dose) begins to converge; however, the image noise increases as well. Transaxial filtration can be used to reduce the image noise, but it blurs the image, which results in changes in dose distribution (smeared), with the degree of severity depending on the FWHM of the filtration and the sphere sizes. Using the DVH RMSE as an objective function allows for joint optimization of both equivalent iterations and filtration simultaneously. Thirty-six iterations with 5.2-mm filtration result in the smallest RMSE across various imaging conditions.

Optimization using the mean RC dose does not take into account the alteration in dose distribution due to changes in image noise, such as increased noise from a higher number of equivalent iterations and reduced noise from a higher filtration FWHM. The converged RC value depended on the scan duration, with a lower RC observed for shorter scan durations, especially for the small (<20 mm) spheres. This may be attributed to the ultra-low signal regimen for ^{90}Y PET compared to that for clinical 18FDG scans. ^{90}Y PET image noise degraded both quantification precision and accuracy. Since spatial filtration reduces the mean RC dose, reconstruction-parameter optimization using the mean dose RC as

the objective function would suggest minimum filtration. However, as shown in Fig 2 and Fig 3, sphere images with no or low filtration resulted in higher errors in DVH.

While it appears that the mean recovery coefficient is too simplistic a metric for the 3D absorbed dose quantification, it is, nonetheless, a direct measure of the quantitative image accuracy (recall that the mean recovery coefficient is the ratio of the estimated value to the true value). While the standard deviation of the mean dose RC can be used to minimize the increased noise from higher number equivalent iterations, it cannot be used to optimize the FWHM of the filtration. Wider FWHM filtration will monotonically result in a lower standard deviation.

In general, the objective function of reconstruction-parameter optimization needs to match the imaging tasks. For dosimetry, where the end points are accurate 3D absorbed dose quantification, the noise distribution plays an important role, as shown in this study. In fact, the asymmetric magnification of noise with lower counts or higher iterations may also perturb the mean value. It is precisely in such situations that the use of DVH RMSE as an objective function is advantageous. As demonstrated here, it allows for joint optimization of both equivalent iterations and filtration simultaneously.

This study was limited to phantom studies using a modified NEMA IEC phantom. Spheres with uniform doses were not true representations of heterogeneous ^{90}Y-microsphere distribution in the tumor. The effects of voxel size and z-axis filtration were not evaluated in this work. Both of these parameters can be optimized to further reduce errors in DVH, but PET spatial resolution is still a limiting factor for calculating accurate DVHs (Fig 2C and Fig 2D).

We only evaluated DVH-based optimization in the GE VPFXS reconstruction algorithm (OSEM with TOF and PSF). The method, however, can be used to optimize reconstruction parameters in other reconstruction algorithms, e.g., the Bayesian penalized-likelihood reconstruction algorithm, where the DVH RMSE can be minimized by adjusting the β and γ parameters instead of the number of equivalent iterations and filtration FWHM.

In our previous study,[27] we found that low-count PET images reconstructed using OSEM caused both random and systematic errors. In a future study, we will use the 3D ^{90}Y-dose map reconstructed using the optimization schema from this study to evaluate both random and systematic errors of the DVH in count-starved ^{90}Y PET studies. This study will help establish the accuracy and precision of quantifying the 3D ^{90}Y dose from PET images.

5. CONCLUSION

Conventional PET image reconstruction optimization aims to increase lesion detection or reduce errors in SUV measurement; both of which are more relevant to diagnostic tasks than to theranostic procedures such as post-therapy ^{90}Y PET imaging. Our proposed objective function of minimizing errors in DVH, which allows for joint optimization of ^{90}Y-PET iterations and filtration to reduce errors in the PET-based volumetric quantification ^{90}Y dose, is more relevant to dosimetry in therapy procedures. We recommend using 36 equivalent iterations with 5.2-mm filtration for ^{90}Y-PET images reconstructed using

VPFXS (GE OSEM with TOF and PSF). The proposed optimization method using DVH as the objection function could be applied more generally to any imaging modality assessing voxel-level quantitative information.

ACKNOWLEDGMENTS

This work was supported in part by NIH/NCI grant R01 CA138986 and by The University of Texas MD Anderson Cancer Center Support Grant CA016672. We thank the Department of Scientific Publication at MD Anderson Cancer Center for assistance with manuscript editing.

CONFLICT OF INTEREST

The authors have no conflicts of interest to disclose.

REFERENCES

[1] R. Salem, K.G. Thurston, B.I. Carr, J.E. Goin, and J.-F.H. Geschwind, Yttrium-90 microspheres: radiation therapy for unresectable liver cancer, J. Vasc. Interv. Radiol. JVIR **13**(9 Pt 2), S223-229 (2002).

[2] R. Salem and K.G. Thurston, Radioembolization with 90Yttrium microspheres: a state-of-the-art brachytherapy treatment for primary and secondary liver malignancies. Part 1: Technical and methodologic considerations, J. Vasc. Interv. Radiol. JVIR **17**(8), 1251–1278 (2006).

[3] R. Cianni, C. Urigo, E. Notarianni, *et al.*, Selective internal radiation therapy with SIR-spheres for the treatment of unresectable colorectal hepatic metastases, Cardiovasc. Intervent. Radiol. **32**(6), 1179–1186 (2009).

[4] B. Gray, G. Van Hazel, M. Hope, *et al.*, Randomised trial of SIR-Spheres plus chemotherapy vs. chemotherapy alone for treating patients with liver metastases from primary large bowel cancer, Ann. Oncol. Off. J. Eur. Soc. Med. Oncol. **12**(12), 1711–1720 (2001).

[5] G. Van Hazel, A. Blackwell, J. Anderson, *et al.*, Randomised phase 2 trial of SIR-Spheres plus fluorouracil/leucovorin chemotherapy versus fluorouracil/leucovorin chemotherapy alone in advanced colorectal cancer, J. Surg. Oncol. **88**(2), 78–85 (2004).

[6] W.A. Dezarn, J.T. Cessna, L.A. DeWerd, *et al.*, Recommendations of the American Association of Physicists in Medicine on dosimetry, imaging, and quality assurance procedures for 90Y microsphere brachytherapy in the treatment of hepatic malignancies, Med. Phys. **38**(8), 4824–4845 (2011).

[7] *Therasphere (TM). BTG Biocompatibles UK Ltd: package insert rev. 14. 2014.*, (n.d.).

[8] *SIR-Sphere (TM). Sirtex Medical Inc: package insert. 2017.*, (n.d.).

[9] J.K. Mikell, A. Mahvash, W. Siman, V. Baladandayuthapani, F. Mourtada, and S.C. Kappadath, Selective Internal Radiation Therapy With Yttrium-90 Glass Microspheres: Biases and Uncertainties in Absorbed Dose Calculations Between Clinical Dosimetry Models, Int J Radiat. Oncol Biol Phys **96**(4):888-896 (2016).

[10] S. Ho, W.Y. Lau, T.W.T. Leung, *et al.*, Partition model for estimating radiation doses from yttrium-90 microspheres in treating hepatic tumours, Eur. J. Nucl. Med. **23**(8), 947–952 (1996).

[11] J.K. Mikell, A. Mahvash, W. Siman, F. Mourtada, and S.C. Kappadath, Comparing voxel-based absorbed dosimetry methods in tumors, liver, lung, and at the liver-lung interface for 90 Y microsphere selective internal radiation therapy, EJNMMI Phys. **2**(1), 16 (2015).

[12] L. Strigari, R. Sciuto, S. Rea, *et al.*, Efficacy and Toxicity Related to Treatment of Hepatocellular Carcinoma with 90Y-SIR Spheres: Radiobiologic Considerations, J. Nucl. Med. **51**(9), 1377–1385 (2010).

[13] E. Garin, L. Lenoir, Y. Rolland, *et al.*, Dosimetry Based on 99mTc-Macroaggregated Albumin SPECT/CT Accurately Predicts Tumor Response and Survival in Hepatocellular Carcinoma Patients Treated with 90Y-Loaded Glass Microspheres: Preliminary Results, J. Nucl. Med. **53**(2), 255–263 (2012).

[14] E. Garin, L. Lenoir, J. Edeline, *et al.*, Boosted selective internal radiation therapy with 90Y-loaded glass microspheres (B-SIRT) for hepatocellular carcinoma patients: a new personalized promising concept, Eur. J. Nucl. Med. Mol. Imaging **40**(7), 1057–1068 (2013).

[15] L. Bester, B. Meteling, N. Pocock, *et al.*, Radioembolization versus Standard Care of Hepatic Metastases: Comparative Retrospective Cohort Study of Survival Outcomes and Adverse Events in Salvage Patients, J. Vasc. Interv. Radiol. **23**(1), 96–105 (2012).

[16] S.A. Gulec, G. Mesoloras, W.A. Dezarn, P. McNeillie, and A.S. Kennedy, Safety and efficacy of Y-90 microsphere treatment in patients with primary and metastatic liver cancer: The tumor selectivity of the treatment as a function of tumor to liver flow ratio, J. Transl. Med. **5**, 15 (2007).

[17] E. Garin, Y. Rolland, J. Edeline, *et al.*, Personalized Dosimetry with Intensification Using 90Y-Loaded Glass Microsphere Radioembolization Induces Prolonged Overall Survival in Hepatocellular Carcinoma Patients with Portal Vein Thrombosis, J. Nucl. Med. **56**(3), 339–346 (2015).

[18] M. Cremonesi, C. Chiesa, L. Strigari, *et al.*, Radioembolization of Hepatic Lesions from a Radiobiology and Dosimetric Perspective, Front. Oncol. **4**, (2014).

[19] G. Sgouros and R.F. Hobbs, Dosimetry for Radiopharmaceutical Therapy, Semin. Nucl. Med. **44**(3), 172–178 (2014).

[20] Y.K. Dewaraja, E.C. Frey, G. Sgouros, *et al.*, MIRD Pamphlet No. 23: Quantitative SPECT for Patient-Specific 3-Dimensional Dosimetry in Internal Radionuclide Therapy, J. Nucl. Med. Off. Publ. Soc. Nucl. Med. **53**(8), 1310–1325 (2012).

[21] S.C. Kappadath, J. Mikell, A. Balagopal, V. Baladandayuthapani, A. Kaseb, and A. Mahvash, Hepatocellular Carcinoma Tumor Dose Response following 90Y-radioembolization with glass microspheres using 90Y-SPECT/CT based Voxel Dosimetry, Int J Radiat. Oncol Biol Phys **102**(2), 451-461 (2018).

[22] M. Sarfaraz, A.S. Kennedy, M.A. Lodge, X.A. Li, X. Wu, and C.X. Yu, Radiation absorbed dose distribution in a patient treated with yttrium-90 microspheres for hepatocellular carcinoma, Med. Phys. **31**(9), 2449–2453 (2004).

[23] W. Siman, J.K. Mikell, and S.C. Kappadath, Practical reconstruction protocol for quantitative 90Y bremsstrahlung SPECT/CT, Med. Phys. **43**(9), 5093–5103 (2016).

[24] R. Lhommel, L. van Elmbt, P. Goffette, *et al.*, Feasibility of 90Y TOF PET-based dosimetry in liver metastasis therapy using SIR-Spheres, Eur. J. Nucl. Med. Mol. Imaging **37**(9), 1654–1662 (2010).

[25] M. D'Arienzo, P. Chiaramida, L. Chiacchiararelli, *et al.*, 90Y PET-based dosimetry after selective internal radiotherapy treatments, Nucl. Med. Commun. **33**(6), 633–640 (2012).

[26] A.S. Pasciak, A.C. Bourgeois, and Y.C. Bradley, A Comparison of Techniques for 90Y PET/CT Image-Based Dosimetry Following Radioembolization with Resin Microspheres, Front. Oncol. **4**, (2014).

[27] W. Siman, O.R. Mawlawi, J.K. Mikell, F. Mourtada, and S.C. Kappadath, Effects of image noise, respiratory motion, and motion compensation on 3D activity quantification in count-limited PET images, Phys. Med. Biol. **62**(2), 448 (2017).

[28] Y.-H. Kao, J.D. Steinberg, Y.-S. Tay, *et al.*, Post-radioembolization yttrium-90 PET/CT - part 2: dose-response and tumor predictive dosimetry for resin microspheres, EJNMMI Res. **3**(1), 1–12 (2013).

[29] A. Balagopal and S.C. Kappadath, Characterization of90Y-SPECT/CT self-calibration approaches on the quantification of voxel-level absorbed doses following90Y-microsphere selective internal radiation therapy, Med. Phys. **45**(2), 875–883 (2018).

[30] M. Elschot, B.J. Vermolen, M.G.E.H. Lam, B. de Keizer, M.A.A.J. van den Bosch, and H.W.A.M. de Jong, Quantitative Comparison of PET and Bremsstrahlung SPECT for Imaging the In Vivo Yttrium-90 Microsphere Distribution after Liver Radioembolization, PLoS ONE **8**(2), (2013).

[31] K.J. Fowler, N.M. Maughan, R. Laforest, *et al.*, PET/MRI of Hepatic 90Y Microsphere Deposition Determines Individual Tumor Response, Cardiovasc. Intervent. Radiol. **39**, 855–864 (2016).

[32] R.G. Selwyn, R.J. Nickles, B.R. Thomadsen, L.A. DeWerd, and J.A. Micka, A new internal pair production branching ratio of 90Y: the development of a non-destructive assay for 90Y and 90Sr, Appl. Radiat. Isot. Data Instrum. Methods Use Agric. Ind. Med. **65**(3), 318–327 (2007).

[33] K.P. Willowson, M. Tapner, The Quest Investigator Team, and D.L. Bailey, A multicentre comparison of quantitative 90Y PET/CT for dosimetric purposes after radioembolization with resin microspheres, Eur. J. Nucl. Med. Mol. Imaging 1–21 (2015).

[34] K. Willowson, N. Forwood, B.W. Jakoby, A.M. Smith, and D.L. Bailey, Quantitative 90Y image reconstruction in PET, Med. Phys. **39**(11), 7153–7159 (2012).

[35] A. Goedicke, Y. Berker, F.A. Verburg, F.F. Behrendt, O. Winz, and F.M. Mottaghy, Study-Parameter Impact in Quantitative 90-Yttrium PET Imaging for Radioembolization Treatment Monitoring and Dosimetry, IEEE Trans. Med. Imaging **32**(3), 485–492 (2013).

[36] T. Carlier, T. Eugène, C. Bodet-Milin, *et al.*, Assessment of acquisition protocols for routine imaging of Y-90 using PET/CT, EJNMMI Res. **3**(1), 11 (2013).

[37] J.M. Martí-Climent, E. Prieto, C. Elosúa, *et al.*, PET optimization for improved assessment and accurate quantification of 90Y-microsphere biodistribution after radioembolization, Med. Phys. **41**(9), 092503 (2014).

[38] K.N. Tapp, W.B. Lea, M.S. Johnson, M. Tann, J.W. Fletcher, and G.D. Hutchins, The Impact of Image Reconstruction Bias on PET/CT 90Y Dosimetry After Radioembolization, J. Nucl. Med. **55**(9), 1452–1458 (2014).

[39] S.C. Kappadath, T. Pan, W.D. Erwin, and O. Mawlawi, Analysis of the dependence of PET/CT quantification on iterative reconstruction parameters, in *IEEE Nucl. Sci. Symp. Conf. Rec. 2007 NSS 07*(2007), pp. 4406–4409.

[40] L. Strigari, E. Menghi, M. D'Andrea, and M. Benassi, Monte Carlo dose voxel kernel calculations of beta-emitting and Auger-emitting radionuclides for internal dosimetry: A comparison between EGSnrcMP and EGS4, Med. Phys. **33**(9), 3383–3389 (2006).

[41] N. Lanconelli, M. Pacilio, S. Lo Meo, *et al.*, A free database of radionuclide voxel S values for the dosimetry of nonuniform activity distributions, Phys. Med. Biol. **57**(2), 517–533 (2012).

[42] W.E. Bolch, L.G. Bouchet, J.S. Robertson, *et al.*, MIRD Pamphlet No. 17: The Dosimetry of Nonuniform Activity Distributions—Radionuclide S Values at the Voxel Level, J. Nucl. Med. **40**(1), 11S-36S (1999).

[43] M. Conti, Focus on time-of-flight PET: the benefits of improved time resolution, Eur. J. Nucl. Med. Mol. Imaging **38**(6), 1147–1157 (2011).

[44] G. Akamatsu, K. Ishikawa, K. Mitsumoto, *et al.*, Improvement in PET/CT Image Quality with a Combination of Point-Spread Function and Time-of-Flight in Relation to Reconstruction Parameters, J. Nucl. Med. **53**(11), 1716–1722 (2012).

LIST OF FIGURES

Fig 1. The sphere volumes of interest were used to quantify the hot spheres dose.

Fig 2. PET images of the modified IEC phantom reconstructed using the number of equivalent iterations (the product of the iteration and subsets) of 12, 24, 36, and 48 **(A)** and post-reconstruction filtration FWHM of 2.6, 5.2, 7.8, and 10.4 mm **(B)**. **(C, D)** The corresponding DVH of the 17-mm sphere (nominal dose 230 Gy) calculated from **(A)** and **(B)**, respectively. The solid black curves indicate the reference DVH, which was calculated using the dose-point-kernel convolution method.

Fig 3. Root mean square errors (RMSEs) in the sphere dose volume histogram (DVH) estimates as a function number of equivalent iterations (the product of the iteration and subsets) and filtration full width at half maximum (FWHM) for a **(A)** 17-mm sphere with a dose of 230 Gy and acquisition duration of 15 min, **(B)** 17-mm sphere with a dose of 37 Gy and acquisition duration of 15 min, **(C)** 37-mm sphere with a dose of 110 Gy and acquisition duration of 15 min, and **(D)** 13-mm sphere with a dose of 230 Gy and acquisition duration of 15 min. The RMSE was calculated as an average of RMSE in 5 noise realizations. The standard errors of RMSE (black vertical error bar) are shown. Using 36 equivalent iterations with 5.2-mm filtration, RMSEs of sphere DVH estimates were consistently among the lowest.

Fig 4. Root mean square errors (RMSEs) of the 17-mm sphere (110 Gy) dose volume histogram (DVH) estimate for various dose threshold ranges. Using the entire range, D_0–D_{100}, resulted in an optimization systematic error in which a low number of equivalent iterations (the product of the iteration and subsets) is preferred to avoid high errors due to noise-degraded images.

Fig 5. Sphere mean dose recovery coefficient (RC) as a function of the number of equivalent iterations (the product of the iteration and subsets) for **(A)** 3 sphere sizes with 3 acquisition durations, **(B)** 3 sphere sizes with 2 sphere-to-background ratios (SBRs), and **(C)** 3 sphere sizes with 2 dose levels and an SBR of 13. The convergence rates of the sphere RC were insensitive to sphere sizes, durations, SBRs, and dose levels; after subset × iterations of 36, all sphere RCs in various imaging conditions reached convergence.

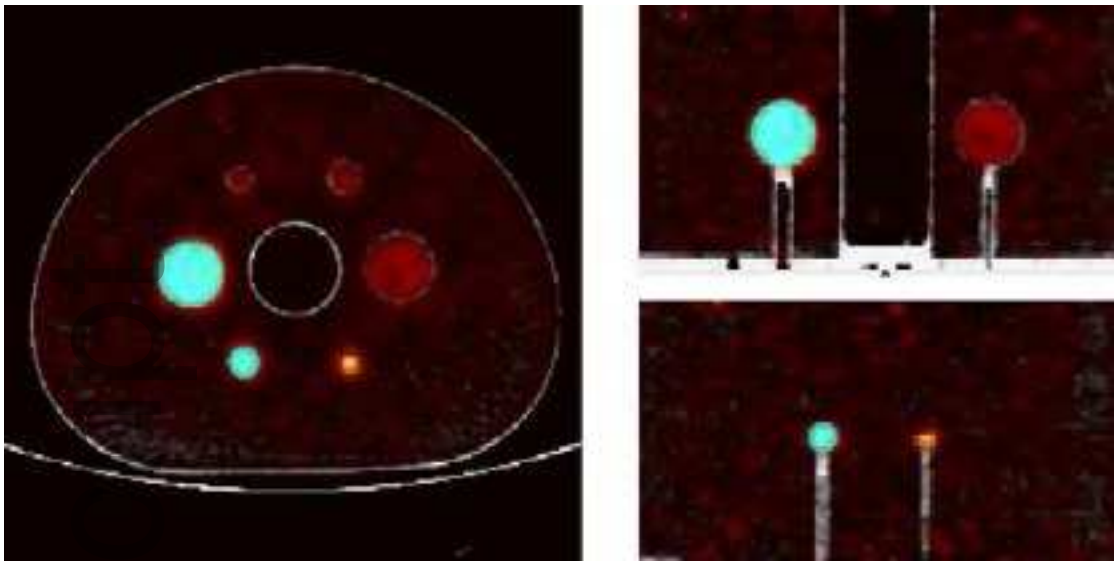

mp_13269_f1.jpg

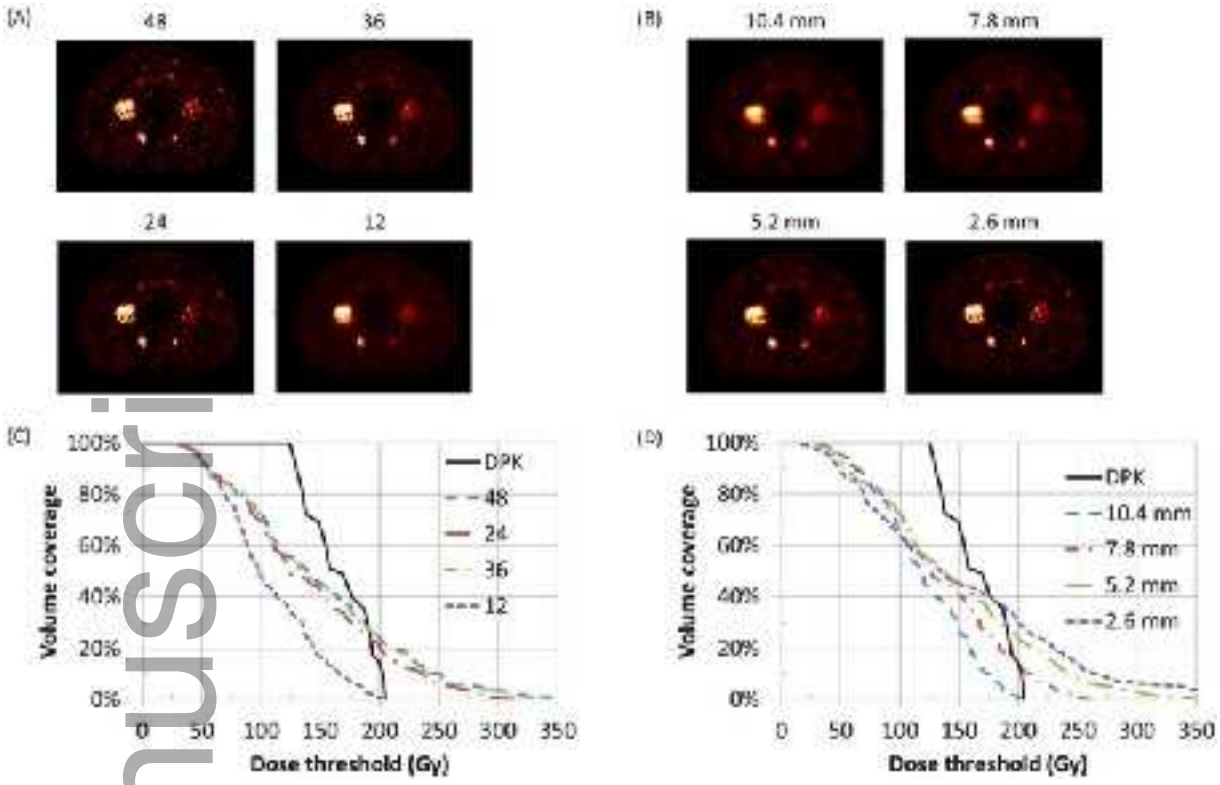

mp_13269_f2.jpg

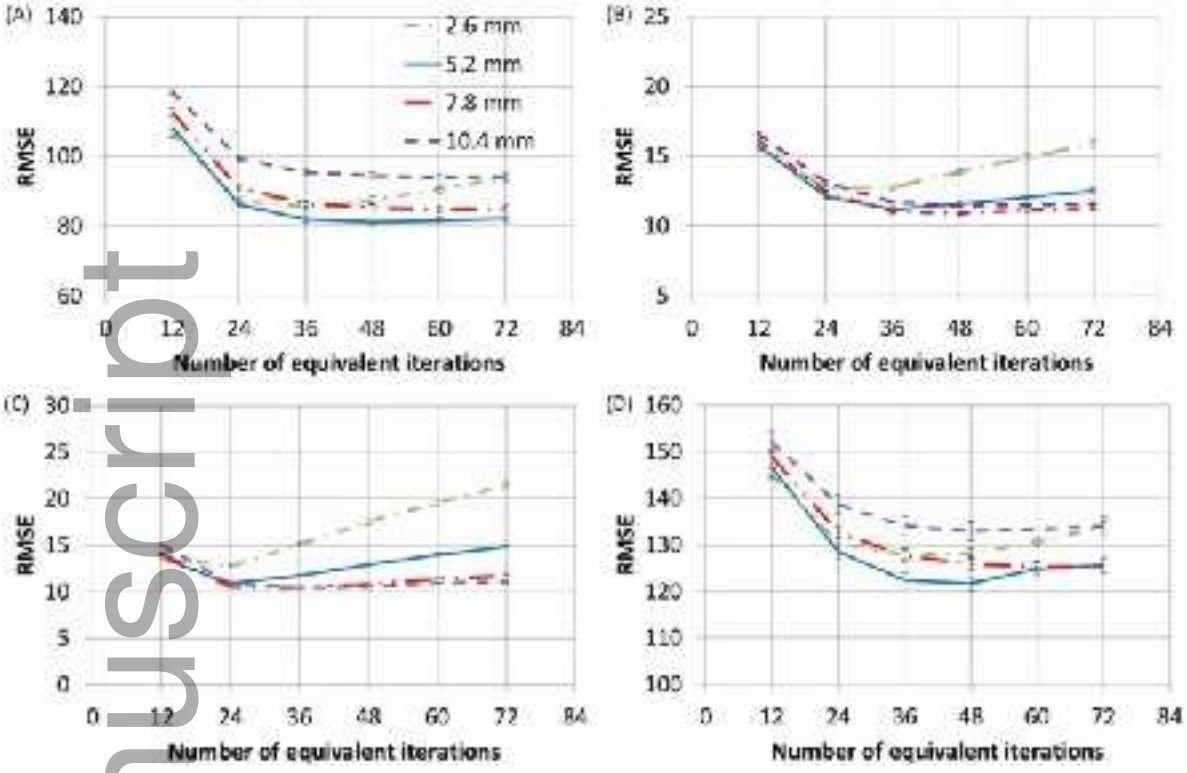

mp_13269_f3.jpg

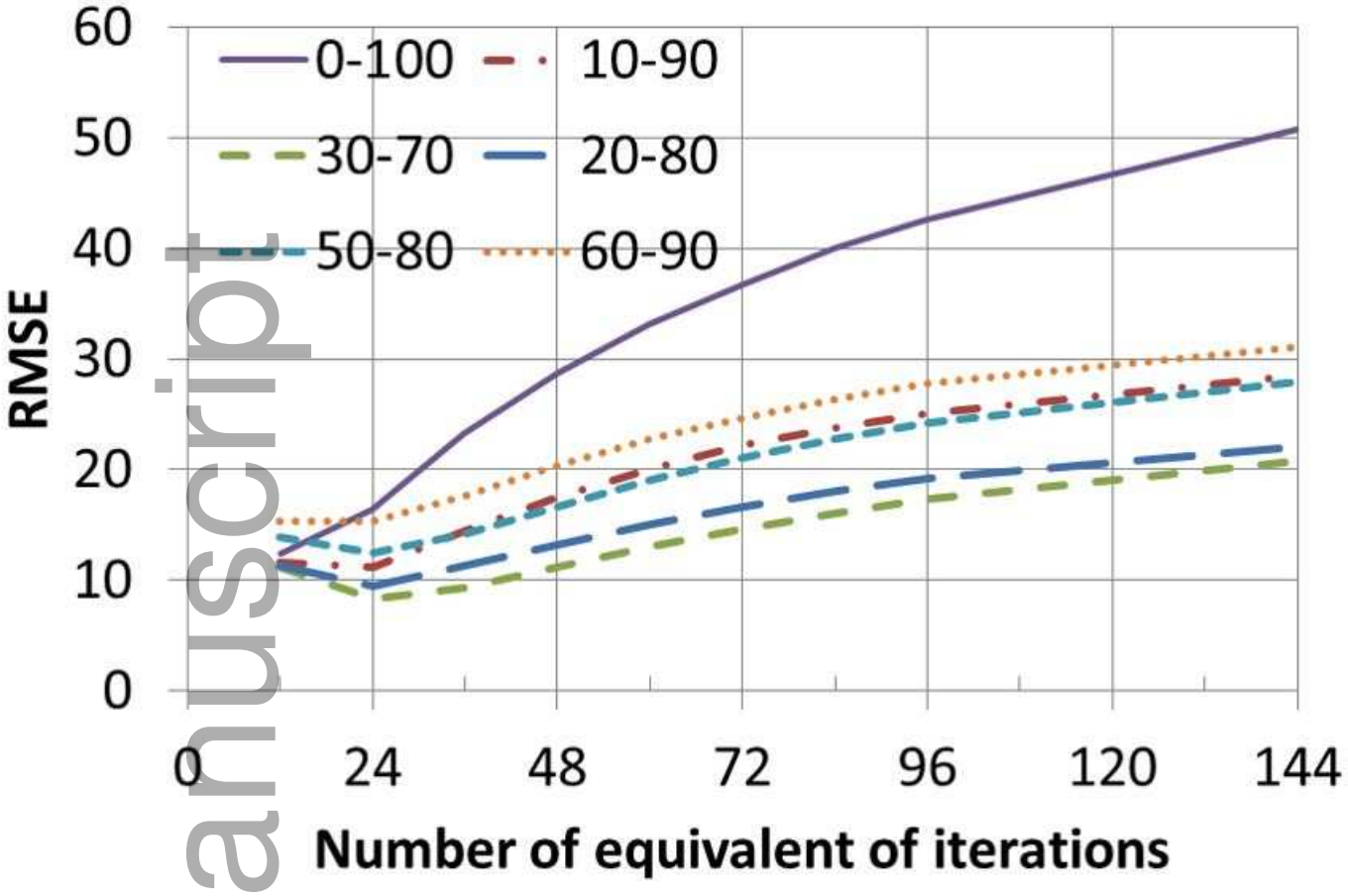

mp_13269_f4.jpg

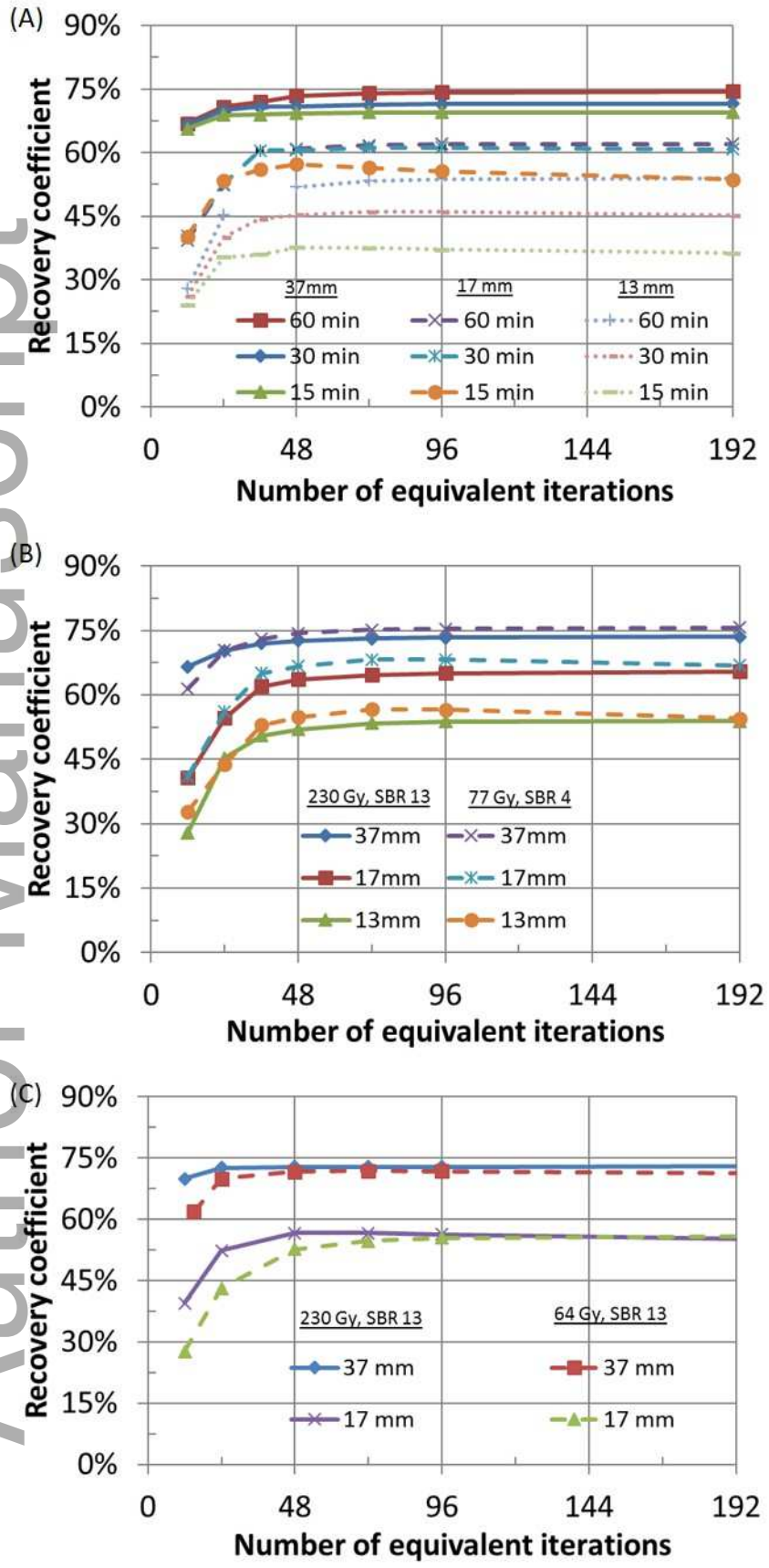

mp_13269_f5.jpg